PHYSICAL REVIEW E **79**, 036315 (2009)

Onset of motion of a partly hidden cylinder in a laminar shear flow

R. Martino,[1] A. Paterson,[2] and M. Piva[1]
[1]*Grupo de Medios Porosos, Facultad de Ingeniería, Universidad de Buenos Aires, Paseo Colón 850 (1063), Buenos Aires, Argentina*
[2]*Departamento de Hidráulica, Facultad de Ingeniería, Universidad de Buenos Aires, Las Heras 2214 (1127), Buenos Aires, Argentina*

(Received 13 May 2008; revised manuscript received 17 February 2009; published 31 March 2009)

In this paper, the onset of motion of an isolated cylinder partially exposed to a shear flow is experimentally investigated. The experiments are performed in a small narrow channel which provides a vertical shear layer flow whose sizes correspond with the channel width. The bottom of the channel is smooth except in the test zone, at long distance from the inlet, where the cylinder is placed with its principal axis perpendicularly directed to the main flow. The geometry of the channel bottom at the test zone is such that the cylinder is partially buried and presents different expositions to the incident flow. In this way, the geometrical constraints imposed by the sediment bed on a single particle in a natural sediment transport situation are reproduced in an idealized context. The results are interpreted in terms of the relation between the particle mobility parameter at the critical condition and the here defined particle burial degree with respect to the bed geometrical constraints β. We emphasize the role played by this burial degree that is dependent on the particle exposure to the incident flow E and the resistance to the motion by mechanical contacts with its surroundings given by the so-called static pivot angle ϕ.

DOI: 10.1103/PhysRevE.79.036315 PACS number(s): 47.85.−g, 45.50.−j, 92.10.Wa

I. INTRODUCTION

The burial degree of one particle resting on a bed of similar particles has been early recognized as a key variable that strongly affects the effective particle mobility due to a fluid stream. A recent and exhaustive revision of this subject can be found in [1], including a detailed discussion about the difference between exposure and protrusion of a given particle.

Several semiempirical approaches have been proposed in order to take the burial degree into account. However, it still remains an open problem how this parameter could be included in a physically meaningful way into the modeling, preserving a well-posed analytical formulation [2]. There is a lack of experimental results supporting the modeling because of the difficulties that arise when dealing with flow turbulence and stochastic distribution of particles on the bed. It is this stochastic nature which leads individual particles to be disposed in different configurations on the surface of the granular bed. In this context, the burial degree will account for the way the individual particles are held by its near neighborhoods.

In this work, we propose a simple experiment to study the initiation of particle motion in a laminar shear flow with the focus on the influence of the burial degree. The experiments were designed in such a way that the problem could be considered two dimensional. In this way, the effects of the lateral diverted flow are avoided so as the initiation of particle motion can be mainly attributed to the relative influence of two forces. One is the fluid force acting on the upstream side of the particle and the other the force due to the bed resistance or friction acting on the downstream side of the particle. In this simplified context, the burial degree can be decomposed into two independent components: the upstream component due to the particle exposure to the incident flow and the downstream component due to the obstruction of contacting particles on its rear side.

Entrainment of particles by a stream is of wide interest in different practical scenarios as, for example, in industrial flows, landslides, and sediment transport by a river or wind. For industrial conduits, it is of primary interest to know the limit values of the flow rate for avoiding entrainment [3] or for reaching transport conditions [4].

Since the pioneering work of Shields, cited by Guo [5] to the present [6], most of the studies have been devoted to investigate the onset of sediment motion under many different conditions with the emphasis in the collective behavior of particles. Several transport models based on the statistical properties of a large number of particles often neglect some features of the one-particle-bed-flow interaction in order to produce a simplified description of reduced complexity [7–9]. Nowadays however, it is clear that the collective behavior of the ensemble in the vicinity of the threshold can be better captured if the behavior of a single particle near the onset is fully understood. This is especially true in the area of numerical simulations where the increased computer capabilities can manage more and better models of the interaction between particle bed and fluid as well as a detailed knowledge of the variables involved in this phenomenon [10]. The influence of particle shape, size, and material on the incipient motion have been extensively studied but it was only recently that the relevance of factors, such as the burial degree, has been identified [1,9].

As was pointed out in [11] the sediment transport is an essentially stochastic phenomenon due to the randomness induced by flow turbulence and those arising from the random characteristic of the bed. However, under laminar flow conditions the randomness of the turbulence disappears and the bed characteristics, such as the size, shape, and position of the particles, becomes the dominant factor inducing transport. Of particular interest are the recent works of [12,13], where the erosion of a bed of spherical particles was studied under laminar flow conditions.

The main objective of this work is to explore experimentally the onset of motion for a single bidimensional prototypical particle, resting on a smooth rigid bed and entirely contained in the laminar boundary layer of the flow. The experiments were carried out in a wide range of particle configurations including symmetric and asymmetric cases.

This paper is structured as follows. Section II contains a description of experimental facilities, Sec. III provides a description of the experiments to measure the velocity profiles in the test section, Sec. IV focuses on the experimental results, Sec. V presents a two-dimensional scheme for the equilibrium of forces at the critical condition, and finally Sec. VI closes with the main conclusions and perspectives.

II. EXPERIMENTAL SETUP

A. Channel and facilities

Based on previous work on small installations for particle-bed-flow interaction studies [8,14–16], the experimental setup used in this work was designed to satisfy the following requirements: (i) the particles should be totally submerged into the bottom boundary layer, (ii) the boundary layer should be laminar, and (iii) the burial degree should be controlled, varied, and measured with reasonable accuracy.

The burial degree and the particle exposure to the incident flow are both of the same order as the particle size. Besides that due to constructive reasons, good control of small lengths could be attained if they are on the order of 1 mm. Taking this into account, the last of the conditions is fulfilled by setting the particle size in between $D_{\mathrm{min}}=2,5$ mm and $D_{\mathrm{max}}=10$ mm. This allows for burial degree variations on the order of half a millimeter or less.

Given the maximum particle size, the first condition is satisfied if the boundary layer thickness δ verifies $\delta > D_{\mathrm{max}}$. Now, for a smooth narrow open channel of rectangular cross section, it was shown in previous works [17] that δ will scale with the width b of the channel if $b < h$, being h as the height of the fluid column. Then, the submergence condition is automatically satisfied if the width of the channel is $b > D_{\mathrm{max}}$ and with the previous value for D_{max}; our choice was finally $b=2$ cm.

Given the width b, the remainder dimensions of the channel were selected to attain a stationary and fully developed laminar boundary layer at a relative short distance from the fluid inlet. The channel was formed by two plates of glass of 130 cm in length, 15 cm in height, and 1 cm in width separated by a 2 cm width piece of perspex, so the maximum flow depth was 8 cm and the width of the channel was then fixed to 2 cm with an uncertainty on the width adjustment all along the channel of less than 2%. The box was assembled using silicon seal on a metallic frame.

The fluid discharge was imposed by a pump connected to a recirculating close circuit, including a bypass circuit with a valve that allowed a precise control of the flow-rate increments (see Fig. 1). The flow rate was measured using a flow rotameter with a maximum uncertainty of about 3%. The input and output of the fluid were achieved with two straight pipes of 1 cm in diameter and 10 cm in length placed at 2 cm from each end. To obtain good fluid distribution, two orifices were made at the submerged end of the pipes, transverse to the flow direction. To ensure symmetry in all the experiments, the orifices positions were adjusted at half height of the fluid.

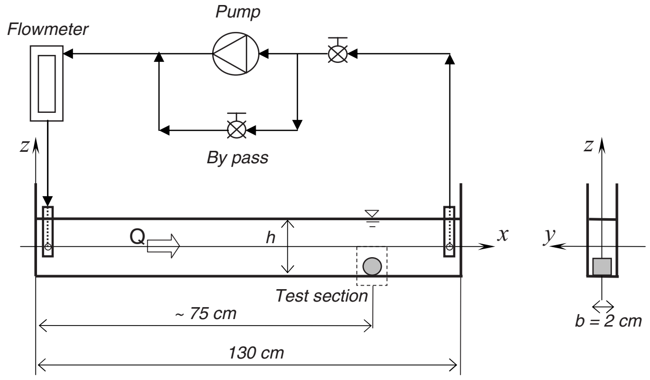

FIG. 1. Experimental setup (not drawn to scale).

Water [density (1000 ± 0004) g/cm^3 and viscosity (0010 ± 0002) g/(cm)] and a water-glycerol solution [50%, density (1130 ± 0005) g/cm^3, and viscosity (0065 ± 0005) g/(cm)] were used as working fluids. The fluid temperature was checked in all the measurements and its value was then used to actualize density and viscosity values.

The height h of the water column was always $h > 4$ cm. In this way the Froude number $\mathrm{Fr}=U/\sqrt{gh} < 0.1$ is small and so the particle interaction with the free surface can be neglected.

The test section was established at a distance L from the inlet larger than the entry length l. This entry length is defined as the distance from the inlet at which the boundary layer is fully developed and was roughly estimated from [18]

$$l/D_h = 0.06\frac{\rho \bar{U} D_h}{\mu}, \tag{1}$$

where $\bar{U}=Q/(bh)$ is the mean flow velocity and $D_h = 2bh/(b+h)$ is the hydraulic diameter of the conduit. The entry length for the worst experimental condition is of about $l=70$ cm. Thus, the test section was established $L=80$ cm from the inlet. More details of the channel facility can be found in [17].

B. Geometry of the buried particles

In a previous work [15], the motion of particles on a rough bed sheared by a viscous flow was studied in narrow channels using spheres of almost the same diameter as the channel width. Thus the particles are compelled to move in a vertical plane and the analysis is considerable simplified. However, in the context of the present work, their configuration is inadequate because the spheres are not fully submerged into the boundary layer as required. To overcome these limitations, the particles were chosen to have cylindrical geometry. The cylinders were made on perspex ($\rho_p = 1.17$ g/cm^3) and aluminum ($\rho_p=2.69$ g/cm^3) of three different diameters ($D=5.0$, 7.5, and 10.0 mm) all of which

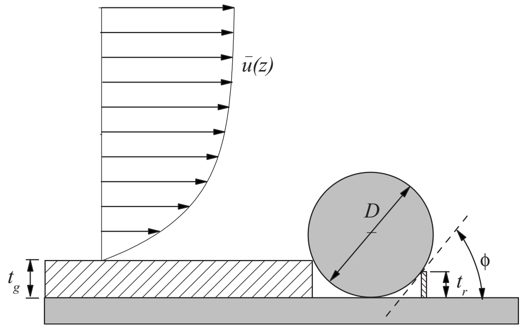

FIG. 2. Scheme of the partially buried cylinder: the uncoupled E and ϕ case.

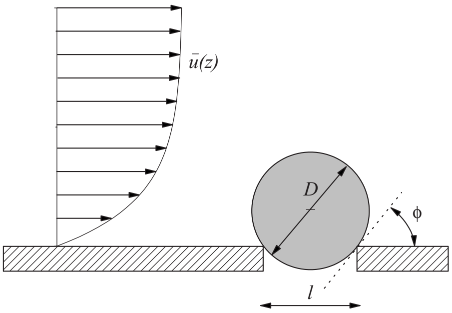

FIG. 3. Scheme of the partially buried cylinder: the coupled E and ϕ case.

were smaller than the thickness of the bottom boundary layer, as required. They were placed at the test section with its axis perpendicular to the flow direction. The cylinder length was b_p=1.8 cm, slightly less than the channel width in order to minimize the unwanted effect of the lateral flow between the channel walls and the cylinder lids.

The local action of the bed on the particle motion was modeled by using blocking elements at both sides of its exposed surface. To model the bed resistance, a thin steel rod of rectangular cross section was embedded immediately downstream of the particle with its mayor axis perpendicular to the flow direction (see Fig. 2). Several rods of heights t_r varying from 0.46 to 3.73 mm were employed in order to simulate different bed friction. The width and the thickness of the rods are 20 mm (equal to the channel width) and 0.8 mm, respectively.

On the other hand, the exposed particle area to the incident flow was varied using a false bottom glass plate of height t_g (2.0, 3.0, and 4.0 mm) with the same channel width which was placed immediately upstream of the particle and all along the channel bottom [19] (see Fig. 2).

Thus, the geometric constraints imposed to the particle can be described using two dimensionless parameters. One is the pivot angle ϕ defined as

$$\phi = \arccos\left(1 - 2\frac{t_r}{D}\right), \tag{2}$$

which is a measure of the bed resistance to the particle motion and the other is the exposure to the incident flow E defined as the ratio between $A_{ef}=b_p(D-t_g)$; the cross-sectional area effectively exposed to the incident flow to $A_T=b_pD$ the total cross-sectional area of the particle,

$$E = 1 - \frac{t_g}{D}. \tag{3}$$

Different combinations of t_r, t_g, and D allowed for the exploration of a wide range of pivot angles ($10° \leq \phi \leq 90°$) and exposure coefficients ($0.5 \leq E \leq 1.0$). In this geometrical configuration, E and ϕ are independent parameters. Another situation was also considered where the cylinder is supported on a slit of variable width l, transverse to the incident flow direction. A schematic of this geometry is shown in Fig. 3.

In this second case, the particle is partially buried on the bed so that the parameters E and ϕ are coupled through the slit width l. In terms of l, the pivot angle reads as

$$\phi = \arcsin\left(\frac{l}{D}\right) \tag{4}$$

and the exposure parameter results

$$E = \frac{1 + \cos\phi}{2}. \tag{5}$$

Thus, by varying the slit width, the pivot angle was varied in the range $5° \leq \phi \leq 80°$ and then the exposure parameter in the range $0.62 \leq E \leq 1$. The main features and the parameters range for the two configurations are summarized in Table I. Cylindrical geometry presents another important advantage when compared to the spherical one which is that cylinders offer a uniform exposure surface for the average flow across the channel gap emphasizing the two-dimensional character of the problem.

TABLE I. Summary of the parameters used in this study.

Configuration	Working fluid	Particle material	D (cm)	H (cm)	E	ϕ (deg)
Decoupled	Water-glycerol	Perpex	0.50 0.75 1.00	4.0 to 6.0	0.20 to 1.00	25 to 90
Buried					0.62 to 1.00	5 to 75
Decoupled	Water	Perpex	0.50 0.75 1.00	4.0 to 6.0	0.20 to 1.00	25 to 90
Buried					0.62 to 1.00	7 to 67
Buried	Water-glycerol	Aluminum	0.50 0.75 1.00	4.0 to 6.0	0.95 to 1.00	10 to 25

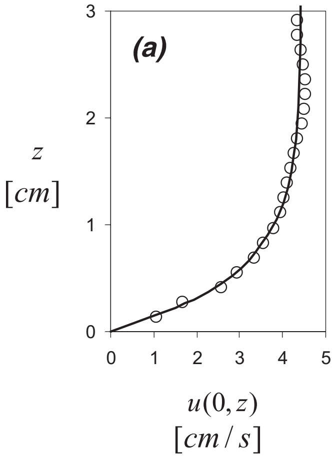

FIG. 4. Near-bottom velocity profiles $u(0,z)$ obtained with PIV technique. (a) water $Q=33.3\ \mathrm{cm^3/s}$, $h=6$ cm, and $\mathrm{Re}_{D_h}=950$; (b) water-glycerol solution $Q=111.8\ \mathrm{cm^3/s}$, $h=6$ cm, and $\mathrm{Re}_{D_h}=470$. Experimental measurements in circles and theoretical profile in continuous line.

III. EXPERIMENTAL VELOCITY PROFILES

The flow field at the test section in the absence of cylinders was characterized using the particle image velocimetry (PIV). A detailed description of the implementation can be found in [17]. Here, only a review of the most important features is given. In all cases, the experimental conditions were fixed in order to ensure a laminar flow.

The flow was seeded with 50 μm radius polyamide particles as tracers illuminated with a vertical continuous green (neodimio-YAG 530 nm) laser sheet located at the channel centerline and images were captured with a charge-coupled device (CCD) camera perpendicular to the laser sheet and connected to a Scion frame grabber. The time gap between consecutive pairs of images was 0.04 s. The test section was typically 10 cm long and 5 cm high corresponding to a frame size of about 600 × 900 pixels. The images were saved in tagged image file format (TIFF) and then processed using SCION IMAGE PC software (Scion Corp., Frederick, MD). Then, a cross-correlation algorithm [20] was applied to twice exposed images to obtain the velocity profile. Examples of velocity profiles for two hydraulic diameter channel D_h based Reynolds number $\mathrm{Re}_{D_h}=\bar{U}D_h/\nu$, with ν fluid kinematic viscosity, are shown in Fig. 4.

A typical profile shows a pronounced boundary layer attached to the bottom of the channel and an internal flow where the tangential velocity is uniform in the vertical direction and acquires its maximum value. The boundary layer thickness was estimated as the vertical distance from the bottom where the tangential velocity reaches 99% of its maximum value $U_{\max}$. The results were plotted against $\mathrm{Re}_L=\rho U_{\max}L/\mu$ the Reynolds number based on the distance L from the inlet to the test section position. As shown in Fig. 5, for $\mathrm{Re}_L<20\,000$, the thickness of the boundary layer is approximately constant and on the order of the channel width.

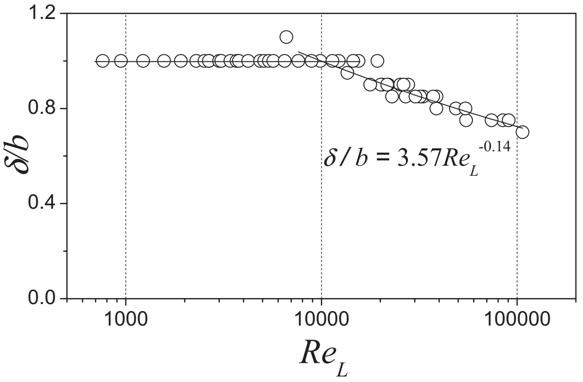

FIG. 5. Boundary layer thickness δ made dimensionless with b as a function of the Re_L.

Data were fitted using the following expression:

$$\frac{\delta}{b}=\begin{cases}1 & \text{if } \mathrm{Re}_L<20\,000\\ 3.57\mathrm{Re}_L^{-0.14} & \text{if } \mathrm{Re}_L>20\,000.\end{cases} \tag{6}$$

The slight decrease of δ for $\mathrm{Re}_L>20\,000$ indicates that the boundary layer is not totally developed. However, it is stationary and fulfill the requirement that $\delta>D$.

On the other hand, the fully developed laminar flow for a closed conduit of rectangular cross section has the form $\mathbf{u}=(u,0,0)$ where u, the longitudinal velocity, can be expressed as [14]

$$u(y,z)=U_{\max}\left\{1-\left(\frac{2y}{b}\right)^2+\sum_{n=1}^{\infty}(-1)^n\frac{32}{[(2n-1)\pi]^3}\right.\\ \left.\times\frac{\cosh\frac{(2n-1)\pi z}{b}\cos\frac{(2n-1)\pi y}{b}}{\cosh\frac{(n-1/2)\pi h}{b}}\right\}, \tag{7}$$

where y and z are the coordinates parallel to the minor and major lengths, respectively, x is the longitudinal direction along the channel, and h and b are the height and width of the channel ($h>b$).

While the above expression is valid for a closed conduit, in this work it was used to fit the lower half part of the flow in an open channel [21]. Superposed to the experimental points, Fig. 4 shows in continuous line the prediction of Eq. (7) when b is replaced by the expression for δ given by Eq. (6). In all cases, from these experimental PIV measurements in the complete range of flow rates and flow heights, we can ensure that the cylindrical particles were fully submerged in the shear flow of the boundary layer.

Considering all the forces acting in the main flow direction x, it is useful to take the average in the transversal direction y,

$$\bar{u}(z)=\frac{1}{b}\int_{-b/2}^{b/2}u(y,z)dy. \tag{8}$$

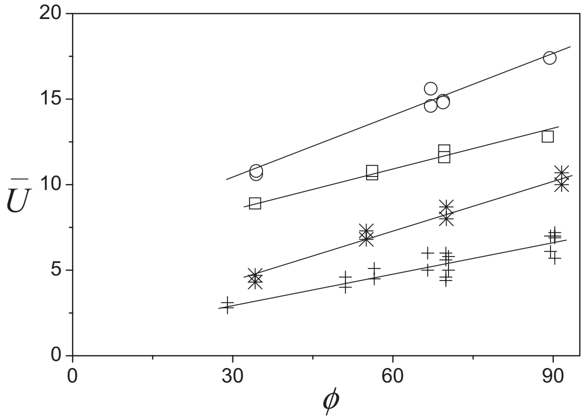

FIG. 6. Critical average velocity $\bar{U}$[cm/s] as a function of ϕ[deg], for the uncoupled E and ϕ case with $D=0.75$ cm. Markers are +: water glycerol, $E=1$; $*$: water glycerol, $E=0.5$; □: water, $E=1$; and ○: water, $E=0.5$. Tendency lines are guides for the eyes only.

This average velocity profile can be considered as the equivalent bidimensional velocity field impinging on the cylinders to produce similar effects as the real one.

IV. EXPERIMENTAL RESULTS

The critical conditions for the incipient motion of the cylinders were determined with the same experimental procedure in both geometrical configurations. For a given fluid depth h and fixed values of the particle parameters E and ϕ, the flow rate Q was progressively increased [1,3] until the cylindrical particle was observed to dislodge from the resting position. The flow-rate increment was established in order to assure quasistationary conditions. In the worst condition, the rate of increment was below 1.6 cm^3/s, which implies mean velocity increments below 0.2 cm/s. Every single measurement was repeated three times to ensure repetitiveness and then we took the average value for Q, with the corresponding experimental uncertainty.

The dimensionless fluid column height h/b was in the range $2<h/b<3$. In all cases, the free surface was verified to remain flat so that the interaction between the particle and the free surface was considered negligible. Figures 6 and 7 summarize the results for $D=0.75$ cm. Similar trends were observed for the other parameter combinations under study. Figure 6 shows the average critical velocity $\bar{U}$ vs the pivot angle ϕ for the case of uncoupled E and ϕ. In this example, the covered range of pivot angles was $30° < \phi < 90°$. Measurements for angles smaller than 30° presented very large dispersion and were not considered confident. In general, the plots show the increasing in the average critical velocity with the pivot angle. It is also shown that the increment of the exposure factor E causes a shift of the curves to lower velocities so that the more exposed the cylinder, the less average velocity needed to initiate the motion. The trend of the results reflects the expected behavior of the system for both parameters. The fluid viscosity also works in the same sense to help the onset of motion, as expected.

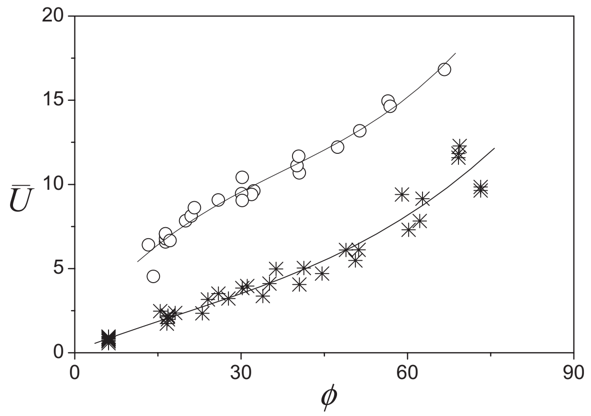

FIG. 7. Critical average velocity $\bar{U}$[cm/s] as a function of ϕ[deg], for the coupled E and ϕ case, with $D=0.75$ cm. Markers are $*$: water glycerol; ○: water. Tendency lines are guides for the eyes only.

For the coupled E and ϕ case, Fig. 7 presents the same trend as earlier with a marked gap separating the two analyzed fluid viscosities. Note that even when both parameters E and ϕ cover a wide range of values, the data points collapse into single curves, for each viscosity. This feature remarks the correctness of the supposed link between E and ϕ for this case.

The above figures give some immediate impression of what may be expected, but they are only a preliminary representation of the rough data. Indeed, the average velocity $\bar{U}$ only represents the mean intensity of the flow in the channel and it is not useful to correctly capture the phenomenology in the close vicinity of the particle.

In order to gain insight about the role played by these parameters, the dimensional analysis was carried out including the whole set of variables affecting the onset of motion. For the critical condition under study, it is assumed that there exists a functional relationship which can be written as

$$f_1\left(\rho,\mu,u,\frac{(\rho_p-\rho)}{\rho},g,D,E,\phi\right)=0, \tag{9}$$

where ρ and μ are fluid density and viscosity, respectively, ρ_p is particles density, g is the acceleration of gravity, and u is a reference velocity measured at height $z=\alpha D$ from the bed level. π theorem leads to a more comprehensive relationship between dimensionless numbers, namely,

$$f_2\left(\frac{\rho u^2}{(\rho_p-\rho)gD},\frac{\rho(\rho_p-\rho)gD^3}{\mu^2},E,\phi\right)=0. \tag{10}$$

The mobility (or Shields) parameter θ is defined as

$$\theta=\frac{\rho u^2}{(\rho_p-\rho)gD} \tag{11}$$

and represents the ratio between the hydrodynamic forces acting to move the particle and the apparent weight of the particle which act in the sense to resist the motion and is frequently used for the evaluation of critical condition for sediment transport [8].

As can be found in literature [8], the reference velocity u can be evaluated as a shear rate-based velocity

$$u = \alpha \dot{\gamma}_b D, \tag{12}$$

being α a proportionality constant less than one [7,8,22]. In the above expression, $\dot{\gamma}_b$ is the width averaged angular deformation rate for an element of fluid calculated from Eq. (8) at the bed level $z=0$,

$$\dot{\gamma}_b = \frac{\partial \bar{u}}{\partial z}(z=0). \tag{13}$$

From Eq. (8) it can be inferred that $\dot{\gamma}_b$ is roughly proportional to the ratio $\bar{U}/b$ [14].

The Galileo number Ga defined as

$$\mathrm{Ga} = \frac{\rho(\rho_p - \rho) g D^3}{\mu^2} \tag{14}$$

is commonly used in sediment deposition and transport studies because it combines the effects of fluid inertia, buoyancy, and viscosity forces. The so-called dimensionless particle diameter D_* used in hydraulics engineering and sediment transport formulae [22–24] is directly related with Ga from the following relation:

$$D_* = \left(\frac{(\rho_p/\rho - 1) g}{(\mu/\rho)^2} \right)^{1/3} D = \mathrm{Ga}^{1/3}. \tag{15}$$

It follows from Eq. (10) that the onset of particle motion depends on the four dimensionless parameters θ, Ga, ϕ, and E. But, following a simple model of forces acting on the particle, it can be shown that ϕ and E are grouped in a unique parameter that accounts for the geometrical linkage existing between the particle and the rough bed. Section V is devoted to develop this point.

V. MODEL OF FORCES FOR THE ONSET OF MOTION

The critical condition for the onset of motion is analyzed here in terms of a balance between the forces acting on the particle. This simple approach, similar to those found in literature [1,7–9,22,25], will expose the relevance of both the static pivot angle ϕ and the exposure parameter E in the threshold of motion.

Figure 8 shows a scheme of the forces for the case of coupled E and ϕ. A particle lying on the bed surface, partially exposed to the fluid stream, is subject—in the flow direction—to the hydrodynamic drag force F_D, and the resistive force due the particle-bed linkage f. In the normal to the flow direction, it is subject to the weight W, the buoyancy B, the normal reaction N, and the hydrodynamic lift force F_L (see Fig. 8). The balance of forces along the flow direction at the limit equilibrium is [1,9,22]

$$F_D = \tan \phi (W - B - F_L) \tag{16}$$

with

$$F_D = C_D \frac{1}{2} \rho u^2 A_{ef}, \tag{17}$$

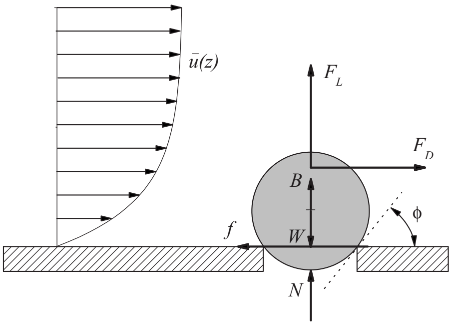

FIG. 8. Sketch of the forces acting on the particle. Forces are: F_D and F_L are drag and lift, $W' = W - B$ and N are the submerged weight and the normal reaction, and f is the bed resistance.

$$W = \frac{\pi}{4} D^2 b_p \rho_p g, \tag{18}$$

$$B = \frac{\pi}{4} D^2 b_p \rho g. \tag{19}$$

Assuming that we are working in the low shear rates regime, the lift force F_L only represents a small fraction of the drag force [26] and then, in the first approximation, it is neglected from Eq. (16).

Regarding the drag force, the majority of the available data on C_D coefficients is given for the regime of large Reynolds numbers and then it does not apply in our case. In the range of the low Reynolds numbers included in the present study (on the order 100 to 500), the results are scarce and limited. Within this range, some data are given in the numerical works of [26,27]. They computed the drag coefficients for cylinders very close to (but never in contact with) a smooth bed. The numerical predictions confine the drag coefficients to the range $2 < C_D < 4$. With the aim of modeling, here, we will ignore the variation of C_D with Re, assuming in the first approximation that it has a constant value in the range of study.

Therefore, by replacing in Eq. (16) the above expressions, it is obtained

$$\frac{\rho u^2}{(\rho_p - \rho) g D} = \frac{\tan \phi}{E} \frac{\pi}{2 C_D}. \tag{20}$$

Similar expressions can be found in literature [1,8,9,25], but in our case it includes explicitly the particle exposure E over the bed. Equation (20) suggests a natural definition for the burial degree coefficient β that combines the roles of E and ϕ as follows:

$$\beta = \frac{\tan \phi}{E}. \tag{21}$$

The values of β are within the theoretical range $0 \leq \beta < \infty$. However, in realistic situations, these extremes values are far from being attained. For example, in the actual experiment, which covers a wide collection of different situations, the range was about $0.2 \leq \beta \leq 6.0$. The role of this parameter is clear; it measures the intensity of the constraints imposed by the bed to the particle motion.

Introducing in Eq. (20) the reference velocity u given by Eq. (12), we obtain

$$\alpha^2 \frac{\rho \dot{\gamma}_b^2 D^2}{(\rho_p - \rho) g D} = \frac{\pi}{2C_D} \frac{\tan \phi}{E} \tag{22}$$

that can be rearranged to give

$$\frac{\mathrm{Re}_p^2}{\mathrm{Ga}} = \frac{\pi}{2\alpha^2 C_D} \beta, \tag{23}$$

where

$$\mathrm{Re}_p = \frac{\rho \dot{\gamma}_b D^2}{\mu} \tag{24}$$

is the so-called particle Reynolds number and Ga is the Galileo number defined before in Eq. (14).

Introducing these parameters into Eq. (10), we arrive to an implicit form relating the three dimensionless numbers characterizing the problem,

$$f_3(\mathrm{Re}_p, \mathrm{Ga}, \beta) = 0. \tag{25}$$

Thus, at the onset of motion the critical particle Reynolds number is a function of the burial degree β and the Galileo number Ga, as can be explicitly deduced from Eq. (23),

$$\mathrm{Re}_p = \left(\frac{\pi}{2\alpha^2 C_D} \right)^{1/2} \mathrm{Ga}^{1/2} \beta^{1/2}. \tag{26}$$

In spite of the simplifying assumptions inherent to the model, the above result of Eq. (26) is interesting because it predicts a direct and simple relationship between the three parameters. The results of Figs. 6 and 7 can be reinterpreted in a more meaningful way by plotting the data sets in terms of this model.

Thus, for the uncoupled case shown in Fig. 6, we can see in Fig. 9(a) that all the data points collapse onto single curves of constant Ga when they are plotted on the $\mathrm{Re}_p - \beta$ plane. In Fig. 9(a) this grouping effect is also evident for the data of the coupled case plotted in Fig. 7, where E and ϕ are dependent variables. In this last case, the fine adjustment of the slit aperture l allowed for a detailed exploration of the small-β region.

At this point, the question arises if β and Ga are also the proper parameters to quantify the variation of Re_p when the values coming from the coupled and the uncoupled configurations are combined in a single plot. The results presented in Fig. 9(b) show that data points are organized around a master curve following the same trend as shown above. In particular, notice the diversity of experimental conditions regarding fluids and particle materials and sizes which are included in the plot of Fig. 9(b). In this sense, the organizing role of Ga is underlined by the wide range of β for which the plots show the overlap of data points coming from the two configurations.

In both cases, the particle Reynolds number for the critical condition Re_p behaves as a monotonically increasing function of β. The growth rate is higher for the smaller values of β, but as β increases the slope increases less steeply showing the typical trend of a power law with exponent less than one. It is worth noting that in the range of $0.2 \leq \beta \leq 1$ are included grain pivot angles of about $20°-40°$, which are common values for noncohesive sediments.

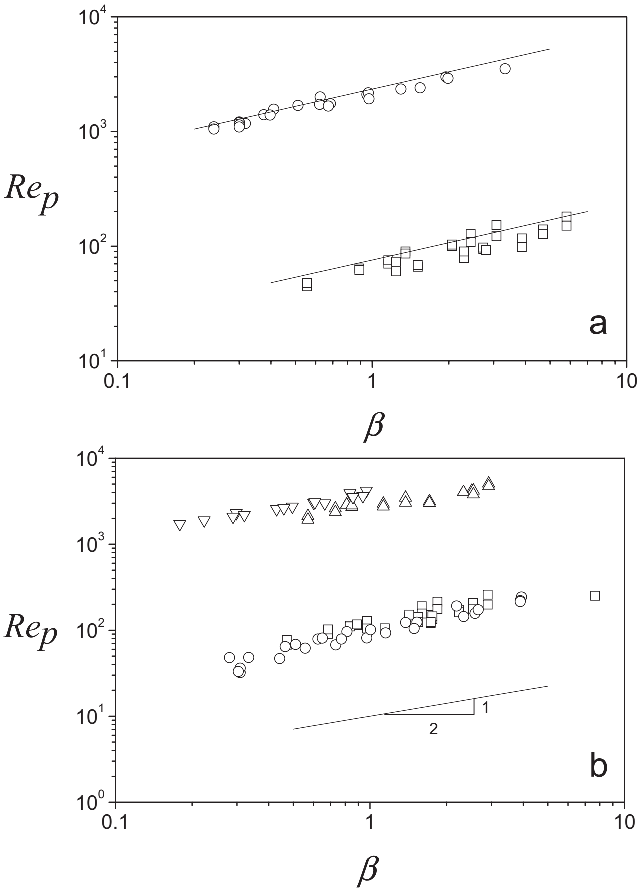

FIG. 9. Re_p vs β parametrized in Ga: (a) □ decoupled case, $\mathrm{Ga}=2.739\times10^3$, $D=0.75$ cm, $\rho_p=1.17$ g/cm^3, and water glycerol; ○ coupled case $\mathrm{Ga}=9.452\ 15\times10^5$, $D=0.75$ cm, $\rho_p=1.17$ g/cm^3, and water. Solid lines correspond to the model of Eq. (26) with $\alpha=0.4$ and $C_D=3$. (b) △ decoupled case, $\mathrm{Ga}=1.850\ 327\times10^6$, $D=1.00$ cm, $\rho_p=1.17$ g/cm^3, and water; ▽ coupled case, $\mathrm{Ga}=2.041\ 094\times10^6$, $D=1.00$ cm, $\rho_p=1.17$ g/cm^3, and water; □ decoupled case, $\mathrm{Ga}=6.988\times10^3$, $D=1.00$ cm, $\rho_p=1.17$ g/cm^3, and water glycerol; ○ coupled case, $\mathrm{Ga}=4.496\times10^3$, $D=0.75$ cm, $\rho_p=1.17$ g/cm^3, and water glycerol.

The plot of Fig. 9(a) also shows the theoretical curves given by Eq. (26). They were obtained by assigning values for C_D and α, which are within the respective ranges. The drag coefficient was an intermediate value in its range of variation ($C_D=3$) and α; the proportionality coefficient in the reference velocity u was set $\alpha=0.4$ which is near the value proposed in [8].

It can be seen that the model curves do not fit perfectly the observed data but they certainly capture the main variation in the trends. The theoretical curves tend to overestimate the experimental data for large values of β. Such discrepancy is, however, within the acceptable limits of the model assumptions. Regarding this point, the lift force may be no longer negligible for the large impinging flow needed to dislodge the cylinder in the large β regime. A finite lift force will act in the sense of reducing the onset of motion which,

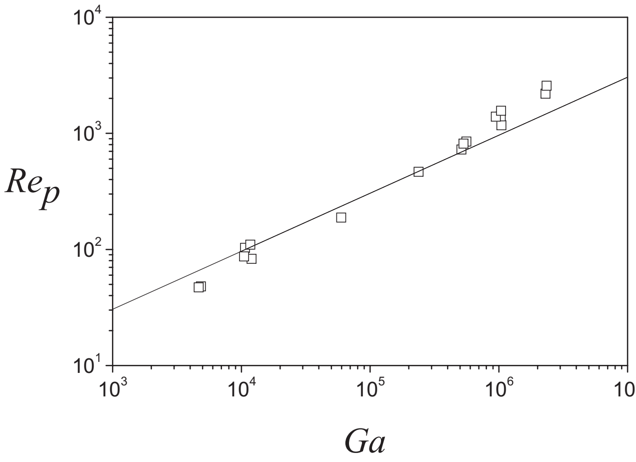

FIG. 10. Dependence of Re_p with Ga for $\beta=0,36$. Solid line corresponds to the model of Eq. (26) with $\alpha=0.45$ and $C_D=3$.

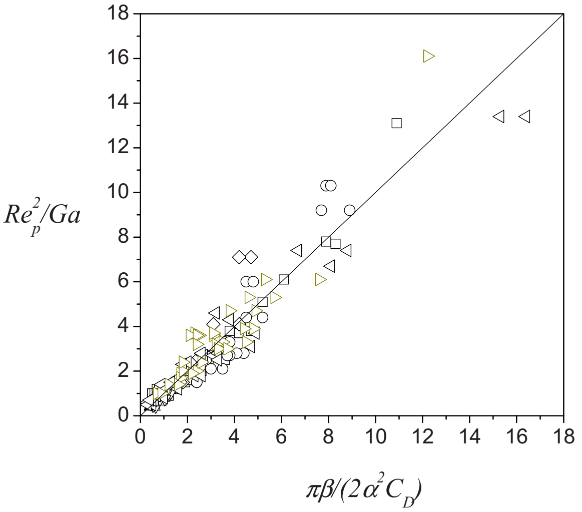

FIG. 11. (Color online) Dependence of $\mathrm{Re}_p^2/\mathrm{Ga}$ with $\pi\beta/(2\alpha^2 C_D)$ combining coupled and decoupled configurations: □ coupled, $\mathrm{Ga}=9.452\,15\times10^5$, $D=0.75$ cm, $\rho_p=1.17$ g/cm^3, and water; ○ decoupled, $\mathrm{Ga}=8.102\,92\times10^5$, $D=0.75$ cm, $\rho_p=1.17$ g/cm^3, and water; △ coupled, $\mathrm{Ga}=5.547\,92\times10^5$, $D=0.75$ cm, $\rho_p=2.79$ g/cm^3, and water glycerol; ▽ coupled, $\mathrm{Ga}=5.411\,95\times10^5$, $D=1.00$ cm, $\rho_p=2.79$ g/cm^3, and water glycerol; ◇ decoupled, $\mathrm{Ga}=2.533\,29\times10^5$, $D=0.50$ cm, $\rho_p=1.17$ g/cm^3, and water; ★ coupled, $\mathrm{Ga}=2.071\,85\times10^5$, $D=0.50$ cm, $\rho_p=1.17$ g/cm^3, and water; ◁ coupled, $\mathrm{Ga}=1.180\,8\times10^4$, $D=1.00$ cm, $\rho_p=1.17$ g/cm^3, and water glycerol; ▷ decoupled, $\mathrm{Ga}=6.988\times10^3$, $D=1.00$ cm, $\rho_p=1.17$ g/cm^3, and water glycerol. Solid line corresponds to the model of Eq. (26) with $\alpha^2 C_D=0.66$.

in turn, will result in a smaller gap between theory and experiments.

In any way, the experimental results of Fig. 9 show a clear relationship between the two variables along the whole range. We highlight this finding because very often in literature [7–9,22] it has been pointed out the influence of ϕ in the scatter of particle mobility. The experimental results presented here suggest that it is not ϕ but the burial degree β is responsible of this scatter.

Following the analysis, we can observe in Fig. 10 that for a given constant value of β, the particle Reynolds number Re_p increases with Ga or, equivalently, with the dimensionless particle diameter.

Recalling on Eq. (23), we note that besides the linear dependence with β, the ratio $\mathrm{Re}_p^2/\mathrm{Ga}$ depends on the parameter $\alpha^2 C_D$ that, in general, is a function of the hydrodynamics close to the particle [7,22]. Nevertheless, as mentioned above, both α and C_D varied over narrow limits and therefore a reasonable description of the phenomenology can be attained if these values are set constants. Figure 11 show that within the 20% of uncertainty, this hypothesis is approximately correct for a wide range of Ga values by taking $\alpha^2 C_D=0.66$. With the drag coefficient assumed previously $C_D=3$, it implies that $\alpha\approx0.45$ or equivalently that the reference velocity u is taken close to $D/2$ from the bed.

As Fig. 11 shows, $\mathrm{Re}_p^2/\mathrm{Ga}$ varies between 0.15 and 15 with β in the range 0.2–6.0. This fact, in turn is indicative that the Shields mobility parameter defined by Eq. (22)

$$\theta=\alpha^2\frac{\mathrm{Re}_p^2}{\mathrm{Ga}} \tag{27}$$

varies between 0.03 and 3.0 approximately. Recent results in the laminar regime have added points to the Shields diagram [8,9,12], indicating that $\theta\approx0.12$ for uniform sediment. If one considers that the representative angle of repose for uniform sediment is $\phi=35°$, it follows from Eqs. (5) and (21) for the symmetrical case that $\beta=0.77$ which is within the range listed above. These results suggest an interesting link between the problem considered here and that of the real world with many particles because even small departures of β from the indicated value that can be expected to occur in a real granular bed will produce significant variations in the values of the mobility factor. Furthermore, the present model may help to explain the significant scatter in the data of the mobility parameter observed in almost of the previous contributions on this subject.

VI. CONCLUSIONS

The conditions for the initiation of motion of a cylinder partially buried and submitted to a shear flow were experimentally studied. The experimental device—a narrow channel suitable for laminar flow studies—as well as the needed auxiliary elements were specially designed to neglect the variations along the width channel direction. In this way, the complex problem concerning the initiation of motion of a particular grain partially buried on a bed of sediment was carried out in the context of a two-dimensional experiment.

In this simplified framework, a large number of different experiments was performed to investigate the role of particle-bed configuration on the onset of motion. The results show that the particle exposure to the incident flow (measured by the exposure factor E) and the resistance to motion due to obstructing elements (measured by the pivot angle ϕ) are the main components of the burial effect.

A simple model based on the equilibrium of forces, which includes the burial effects and the hydrodynamics forces on the cylinder, showed us that the simultaneous effects of E and ϕ can be resumed in a single parameter measuring the overall burial effect $\beta = \tan \phi / E$.

In addition, another parameter, the Galileo number Ga, which accounts for the ratio between the gravity-buoyancy and viscosity effects naturally arise from dimensional analysis. The Galileo number completes the set of dimensionless numbers needed to describe the phenomenon.

Data points on the plots of Re_p vs β show a marked tendency to collapse on single master curves in all the range of study. This result supports the assumption that β is the proper parameter to describe the constraints on the particle motion imposed by the irregular bed.

In spite of the crudeness of the model, the theoretical curves follow the experimental results reasonable well. An interesting point to mention is that the adjustable parameters assumed values within the expectable range of physical meaning. All of these findings provide support in favor of the hypothesis for the model presented here. This model has been proven to be helpful to understand the underlying mechanisms of motion initiation in the two-dimensional case and its application should be limited to the analysis of this simple case. The more realistic understanding of the motion initiation in fluvial hydraulics lies out of the scope of this study; it should be addressed within the framework of a complex three-dimensional problem. Nevertheless, the simple approximation presented here can be taken as an alternative guide for future studies.

ACKNOWLEDGMENT

R.M. acknowledges support from the Fundacion YPF, Buenos Aires, Argentina.

---

[1] A. Armanini and C. Gregoretti, Water Resour. Res. **41**, W12431 (2005).

[2] J. Jarvela, *Flow Sediment Vegetation Interaction: Research Challenges: River Flow 2006* (Taylor and Francis Group, London, 2006).

[3] P. Stevenson, R. B. Thorpe, and J. F. Davidson, Chem. Eng. Sci. **57**, 4505 (2002).

[4] H. Kalman, A. Satran, D. Meir, and E. Rabinovich, Powder Technol. **160**, 103 (2005).

[5] J. Guo, in *Hunter Rouse and Shields Diagram*, Advances in Hydraulics and Water Engineering, Proceedings of the 13th Congress of the IAHR APD, edited by J. Junke Guo (World Scientific, Singapore, 2002), pp. 1096–1098.

[6] L. C. Van Rijn, J. Hydraul. Eng. **133**, 649 (2007).

[7] C. H. Ling, J. Hydraul. Eng. **121**, 472 (1995).

[8] M. Pilotti and G. Menduni, J. Hydraul. Res. **39**, 115 (2001).

[9] U. C. E. Zanke, Int. J. Sediment Res. **18**, 17 (2003).

[10] J. Heald, I. McEwan, and S. Tait, Philos. Trans. R. Soc. London, Ser. A **362**, 1973 (2004).

[11] N. Cheng, Adv. Water Resour. **27**, 937 (2004).

[12] M. Ouriemi, P. Aussillous, M. Medale, Y. Peysson, and E. Guazzelli, Phys. Fluids **19**, 061706 (2007).

[13] A. Lobkovsky, A. Orpe, R. Molloy, A. Kudrolli, and D. Rothman, J. Fluid Mech. **605**, 47 (2008).

[14] P. Gondret, N. Rakotomalala, M. Rabaud, D. Salin, and P. Watzky, Phys. Fluids **9**, 1841 (1997).

[15] T. Bohm, P. Frey, C. Ducottet, C. Ancey, M. Jodeau, and J. Reboud, Exp. Fluids **41**, 1 (2006).

[16] F. Charru, H. Mouilleron, and O. Eiff, J. Fluid Mech. **519**, 55 (2004).

[17] R. Martino, A. Paterson, and M. Piva, Am. J. Phys. **75**, 833 (2007).

[18] R. W. Fox and A. T. McDonald, *Introduction to Fluid Mechanic* (Wiley, NY, 1994), p. 305.

[19] S. Cokgor, Ocean Eng. **29**, 753 (2002).

[20] R. Gurka, A. Liberzon, D. Hefetz, D. Rubinstein, and U. Shavit, *Computation of Pressure Distribution Using PIV Velocity Data*, 3rd International Workshop on Particle Image Velocimetry, Santa Barbara, California (1999).

[21] S. E. Coleman and B. Eling, J. Hydraul. Res. **38**, 331 (2000).

[22] L. C. Van Rijn, *Principles of Sediment Transport in Rivers, Estuaries, and Coastal Seas* (Aqua Publications, Amsterdam, 1993).

[23] P. Y. Julien, *Erosion and Sedimentation* (Cambridge University Press, New York, 1995).

[24] *Sedimentation Engineering: Processes, Measurements, Modeling, and Practice*, ASCE Manual No. 110, edited by M. García (ASCE, Reston, VA, 2008).

[25] N. A. Marsh, A. W. Western, and R. B. Grayson, J. Hydraul. Eng. **130**, 616 (2004).

[26] L. Zovatto and G. Pedrizzetti, J. Fluid Mech. **440**, 1 (2001).

[27] B. Stewart, K. Hourigan, and M. Thompson, Phys. Fluids **18**, 111701 (2006).